Electronic Supplementary Information

A rocking-chair aqueous aluminum-ion battery based on organic/inorganic electrode

Beibei Yang, Yongkang Wang, Haifeng Bian, Yulin Zhang, Yanyan Du, Hongbin Lu* and Duan Bin*

School of Chemistry and Chemical Engineering, Nantong University, Nantong, Jiangsu, 226019, P.R. China.

*Corresponding authors

E-mail: luhb@nju.edu.cn; dbin17@fudan.edu.cn

1. Experimental Section

1.1 Synthesis of porous Ni-PBA: A typical co-precipitation method was applied to prepare the porous Ni-PBA ($K_2NiFe(CN)_6 \cdot xH_2O$). Specifically, $K_4Fe(CN)_6 \cdot 3H_2O$ (3 mmol, 99.0 %, Aladdin) and KCl (12 g, 99.8%, Aladdin) were dissolved in 150 mL deionized (DI) water with stirring for 20 min to produce the transparent solution, which is denoted as A solution. At the same time, $NiCl_2 \cdot 6H_2O$ (6 mmol, 98.0%, Aladdin) was dissolved in another 150 mL DI water, following by a continuous stirring for 30 min to form solution B. To complete the partial substitution of Ni for Fe, the solution A was dropwise added into solution B with magnetic stirring under 70 °C for 2 hours, and then the mixture was aged for 24 h to get the precipitate. The obtained product was filtered by DI water and ethanol for several times and dried in an oven at 60 °C.

1.2 Synthesis of pyrene-4,5,9,10-tetraone (PTO): The organic solid of PTO was prepared by a reported method [1]. 5 g of pyrene (25.4 mmol, 99.0%, Sigma-Aldrich) were dissolved in 100 mL of CH_2Cl_2 (99.0% Sigma-Aldrich), and then 100 mL acetonitrile (99.0 %, Aladdin) solution, followed by adding 44.5 g $NaIO_4$ (207.9 mmol, 99.8 %, Aladdin), 125 mL DI water and 0.64 g of $RuCl_3 \cdot xH_2O$ (3.1 mmol, 99.98%, Sigma-Aldrich), successively. The dark brown mixture was heated at 40 °C overnight, and then the organic solvents were removed by rotary evaporation treatment. After the solid was filtrated and rinsed by DI water, the dark green cake powders were obtained after dried at 60 °C in air. The pure golden needle-like product PTO was produced by the column chromatography (using CH_2Cl_2 as mobile phase).

1.3 Physical Characterization: The morphology and microstructure of Ni-PBA and PTO were observed by a HitachiS-3400 Scanning electron microscopy (SEM) instrument and ThermoFisher Scientific Talos F200x G2 transmission electron microscopy (TEM) equipment. The as-prepared Ni-PBA samples were characterized by a Bruker D8 endeavor X-ray diffractometer (XRD), equipped with Cu Kα (λ = 0.15405 nm) radiation (40 kV, 40 mA). Thermogravimetric analysis (TGA) was carried out on PerkinElmer TGA 7 analyzer at a heating rate of 10 °C min^{-1}, and nitrogen was used as a protective gas. Fourier transform infrared spectroscopy (FTIR) were conducted on a Nicolet 6700 FTIR spectrometer instrument using a KBr pellet. Specific

surface area and porosity analysis was characterized from adsorption and desorption isotherms were performed by a Quantachrome ASiQwin. X-ray photoelectron spectroscopy (XPS) was carried out via a XSAM800 Ultra spectrometer.

1.4 Electrochemical Characterization: The electrochemical performance of Ni-PBA and PTO electrode was evaluated by using a typical three-electrode system, which include the working electrode, active carbon (AC) counter electrode and saturated calomel electrode (SCE) as the reference electrode. The working electrode was fabricated by compressing a mixture of the active materials (Ni-PBA or PTO), conductive material (Ketjen Black, KB) and polytetrafluorethylene binder (PTFE, 20 wt. %) in the weight ratio of 6:3:1 onto a titanium mesh. The area of the cathode and anode electrode was controlled to be 0.64 cm^2, and the loading mass of active materials was ~3 mg cm^{-2} for Ni-PBA cathode and ~1 mg cm^{-2} for PTO anode. A full aqueous AIBs with PBA anode and Ni-PBA cathode was assembled in an open environment, the volume of electrolyte of full cell was controlled to be ~80 μL. Cyclic voltammetry (CV) and electrochemical window of the electrodes were carried out by a CHI760E electrochemistry workstation. Galvanostatic charge/discharge (GCD) and cycling performance measurements were used LAND CT2001A battery test system (Wuhan LAND electronics Co., Ltd).

1.5 The assemble of full aqueous AIBs.

A fully sealed aqueous Al-ion battery with Ni-PBA cathode and PTO anode was assemble in an open environment, the photo images of this batteries were shown in Figure S16. The anode and cathode active materials were suppressed in titanium mesh, glass fibre was used as the separator, and bespoke mode battery was used the sealed battery test. According to the obtained capacities and their retention through the three-electrode system, the specific capacity (mAh) of the anode and cathode for the full aqueous battery was set as 1.1:1. Finally, the current density (A g^{-1}) and the capacity (mAh g^{-1}) were calculated based on the total weight of both cathode and anode material.
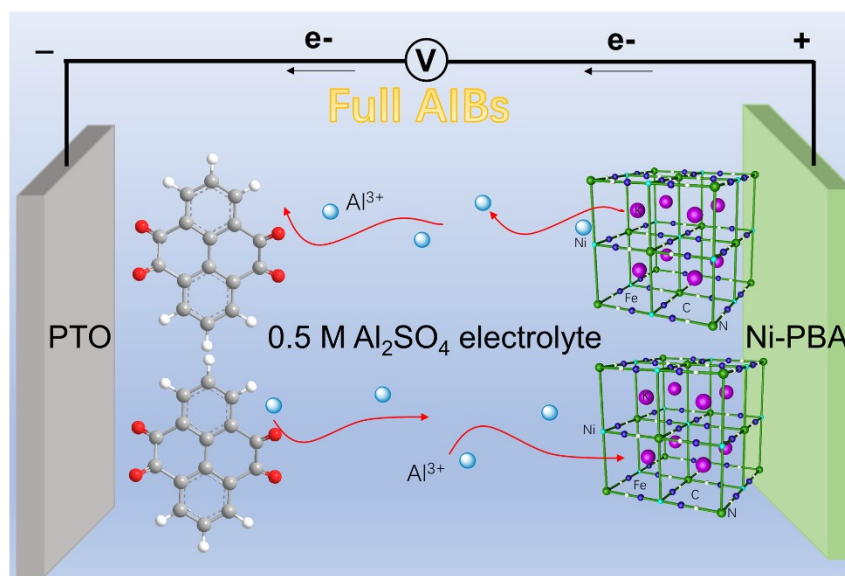
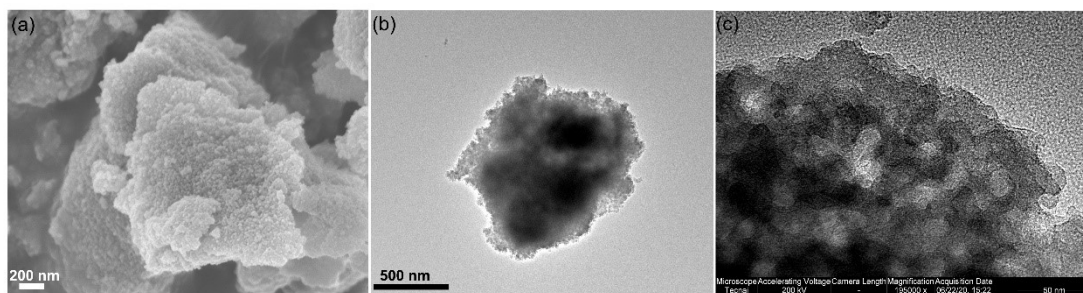**Figure S1.** A schematic of this rocking-chair aqueous AIBs based on the Ni-PBA cathode and PTO anode.

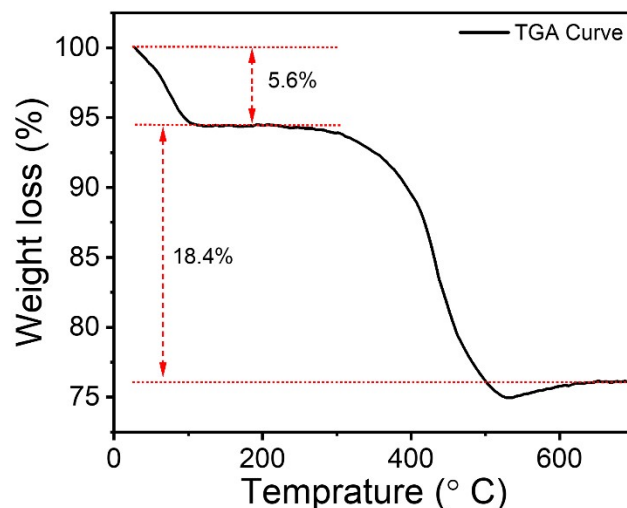**Figure S2**. (a) SEM and (b, c) TEM images of the synthesized Ni-PBA sample.

Figure S3. TGA curve of Ni-PBA.(The Ni-PBA sample first showed a slight weight loss of 5.6% at a temperature below 200 °C due to a release of free adsorbed water, and then exhibited a continuous weight loss of 18.4% from 200–600 °C corresponding to a release of water molecules from the interlayer space; these results revealed that the full formula of Ni-PBA could be represented as $K_2NiFe(CN)_6 \cdot 4.34H_2O$.)
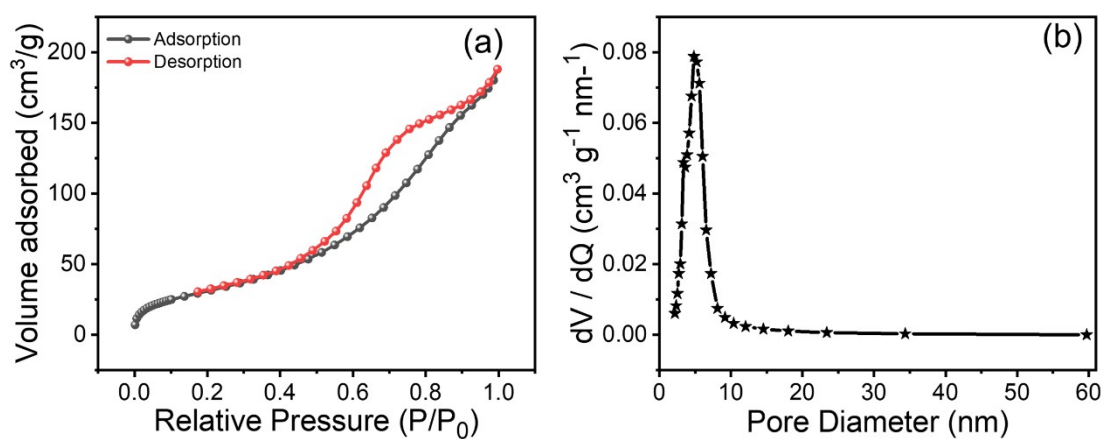

Figure S4. (a) Nitrogen adsorption-desorption isotherm and (b) the corresponding pore size distribution of the porous Ni-PBA.
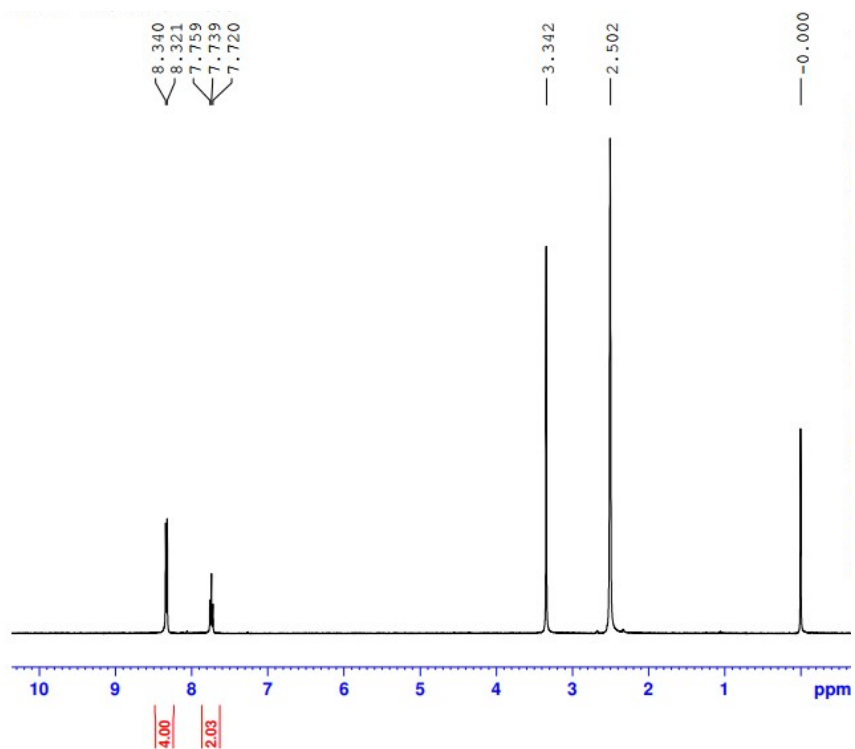
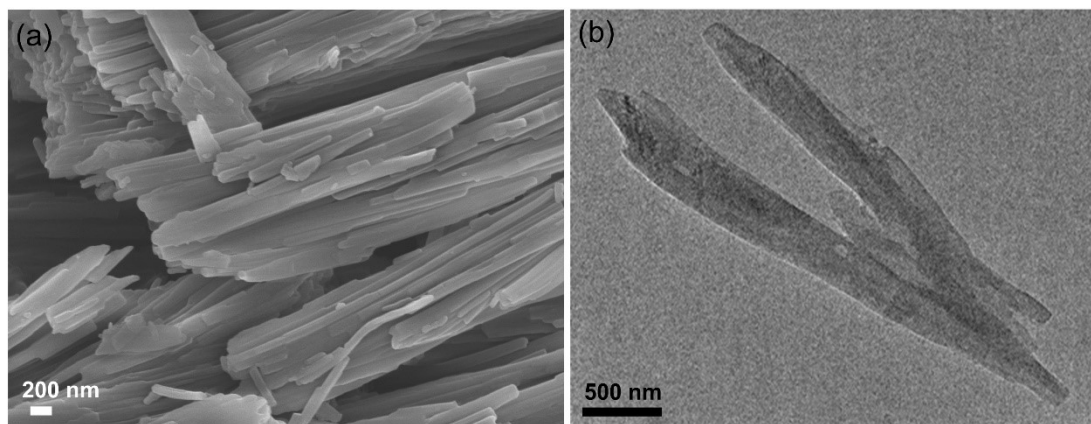**Figure S5.** 1 H NMR (400 MHz, DMSO) of PTO.

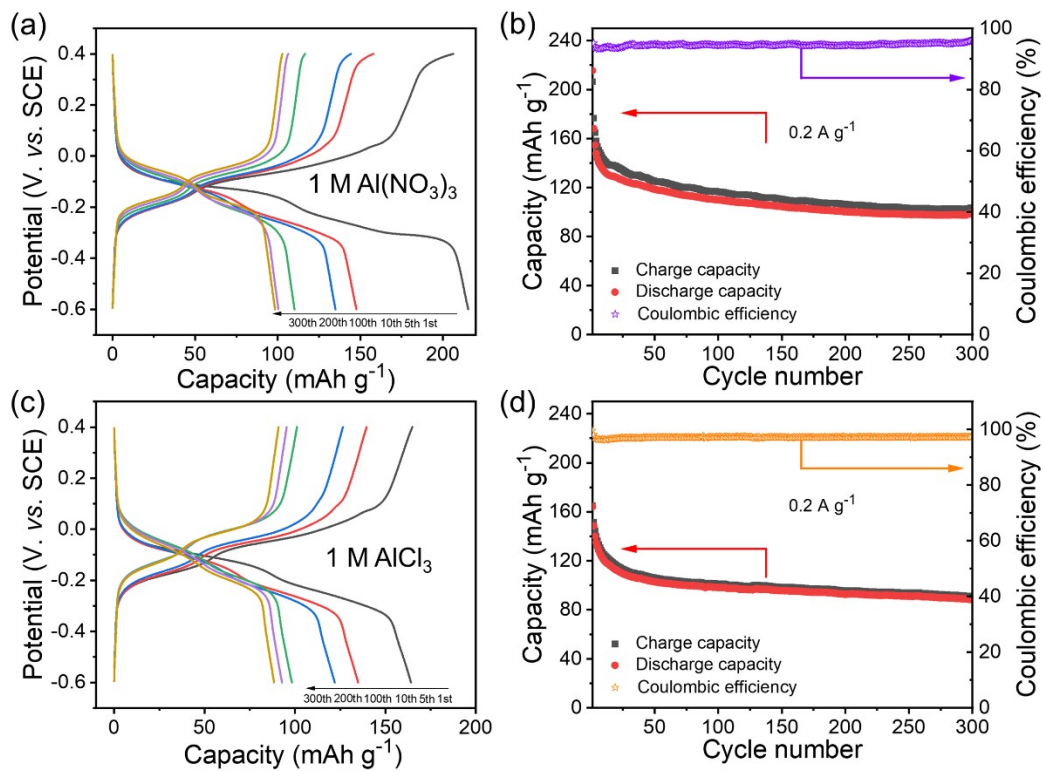**Figure S6.** (a) SEM and (b)TEM images of PTO powder.

Figure S7. (a, b) Galvanostatic charge-discharge curves and the corresponding cycle performance of PTO anode in 1 M $Al(NO_3)_3$ solution. (c, d) GCD curves and the corresponding cycle performance of PTO anode in 1 M $AlCl_3$ solution.
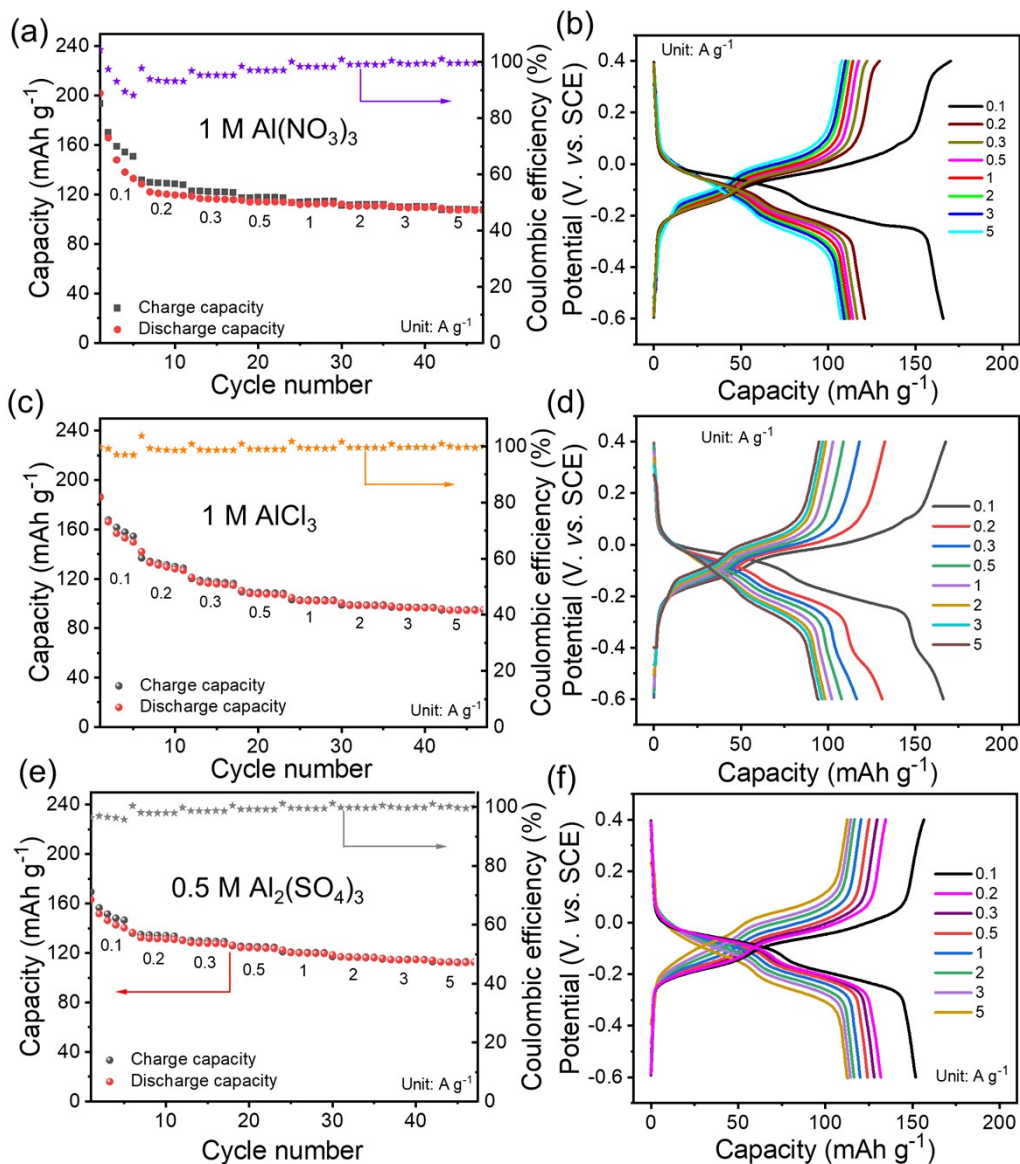
Figure S8. (a, c, e) Rate performance and (b, d, f) the corresponding GCD curves recorded at various rates of PTO anode in 1 M Al(NO$_3$)$_3$, 1 M AlCl$_3$ and 0.5 M Al$_2$(SO$_4$)$_3$ solution. (Versus the discharge capacity at 0.1 A g^{-1}, only 63% of the capacity is remained at 5 A g^{-1} in 1 M Al(NO$_3$)$_3$ solution, and 56% of the capacity is gained 5 A g^{-1} in 1 M AlCl$_3$ solution)
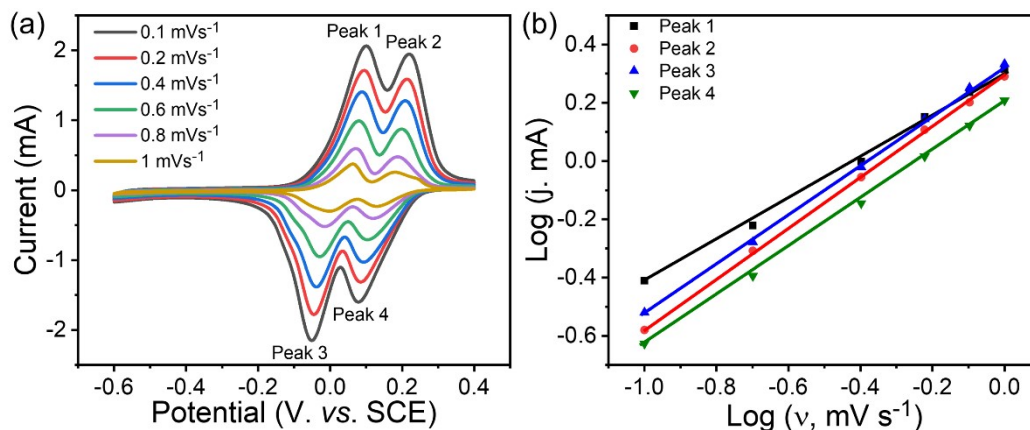
Figure S9. (a) CV curves at different scan rates and (b) corresponding log I versus log v of the PTO anode in 0.5 M $Al_2(SO_4)_3$ solution (Since the enhanced polarization, the oxidation and reduction peaks shifted to higher and lower potentials along with the increased scan rate, respectively. The measured peak current (i_p) at a fixed potential obeys a power lay relationship with the scan rate (v), which can be described as follows, $i_p=av^b$, where a and b are parameters [2]. The calculated b value is 0.73, 0.87, 0.86 and 0.84 for peak 1, peak 2, peak 3 and peak 4, respectively, indicating a fast kinetics for Al^{3+} storage).
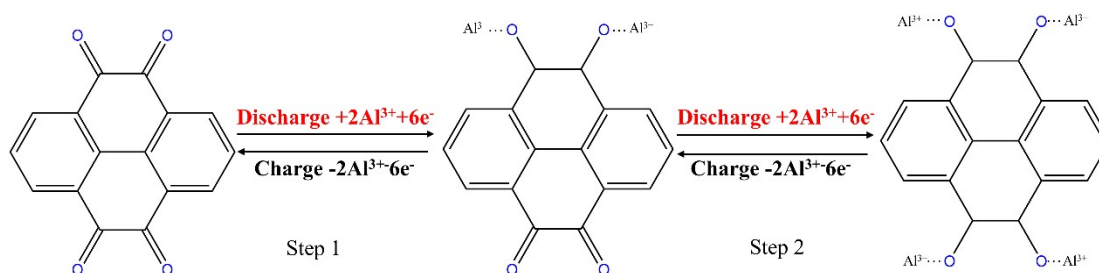

Figure S10. Possible reversible electrochemical redox mechanism of PTO anode.
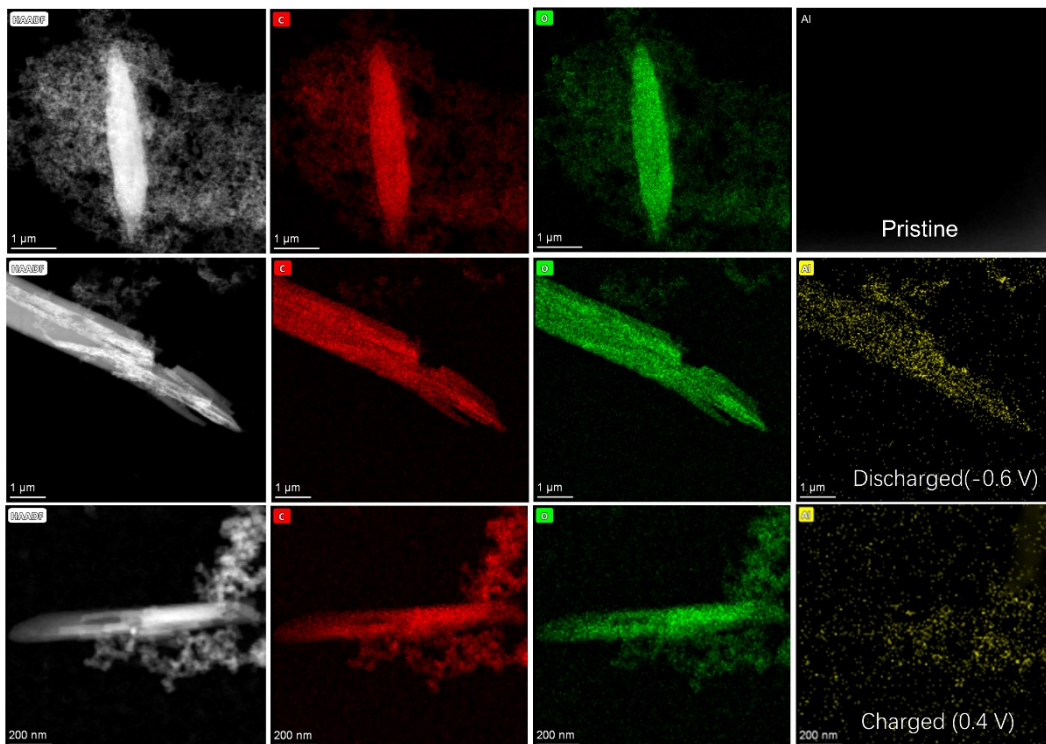
Figure S11. EDS mapping of C, O and Al elemental distributions on PTO anode at pristine and fully discharged (-0.6 V) and fully charged (0.4) states.
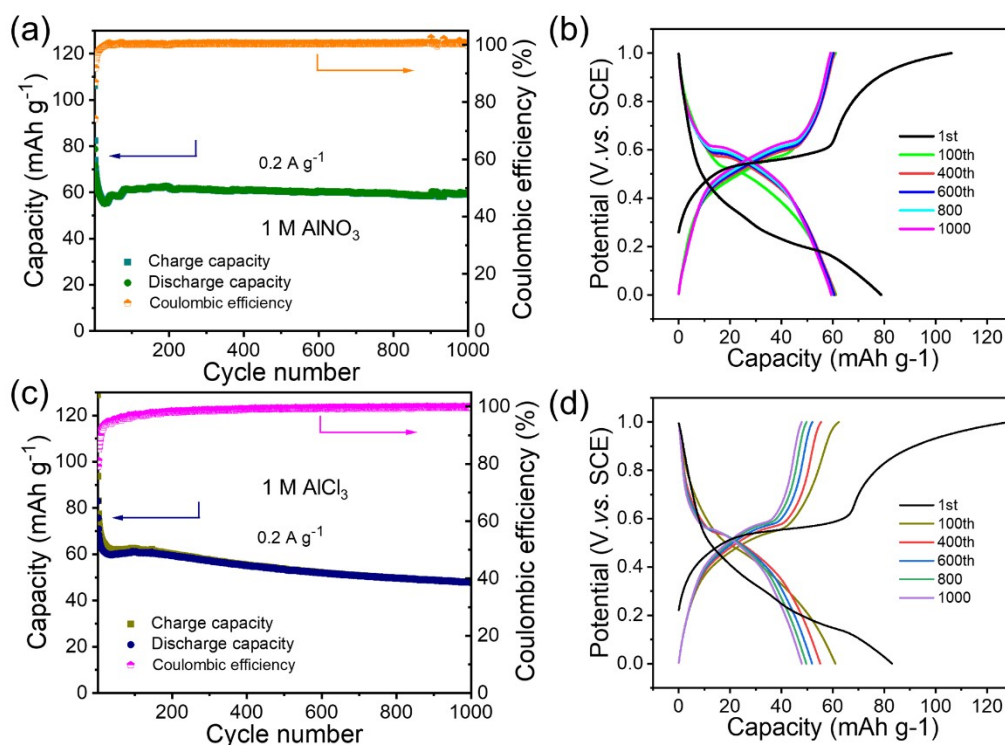

Figure S12. (a, c) Cycling performance and (b, d) the corresponding GCD curves recorded at different cycles of Ni-PBA cathode in 1 M Al(NO$_3$)$_2$ and 1 M AlCl$_3$ solution.
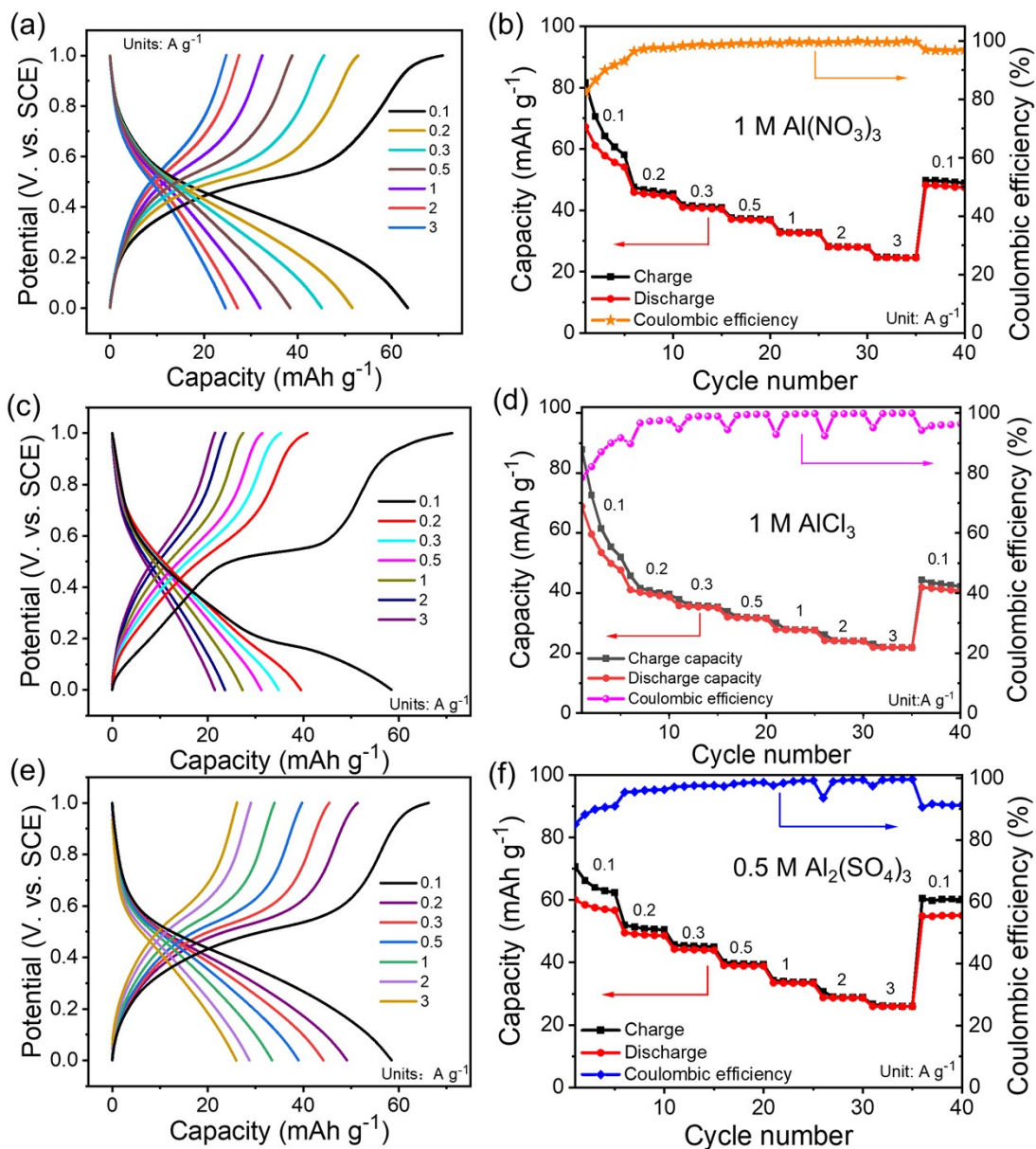
Figure S13. (a, c, e) GCD curves and (b, d, f)the corresponding rate performance recorded at various rates of Ni-PBA cathode in 1 M $Al(NO_3)_2$ and 1 M $AlCl_3$ solution (In 0.5 M $Al_2(SO_4)_3$ solution, the discharge capacity of 24.6 mAh g⁻¹ is obtained at 3 A g⁻¹ with retention of 44.4% towards the capacity at 0.1 A g⁻¹, which is higher than that the value of 38.8 % and 36.7 % in 1 M $Al(NO_3)_3$ and 1 M $AlCl_3$ solution).
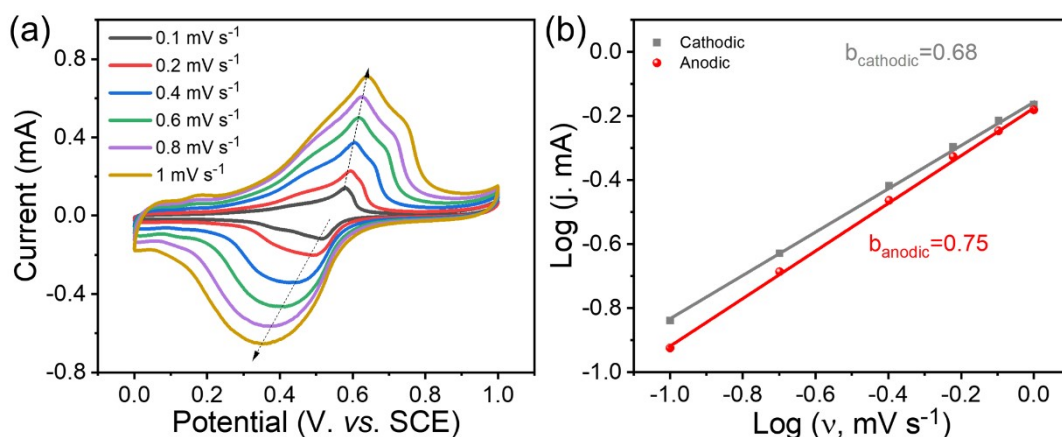
Figure. S14. (a) CV curves at different scan rates and (b) corresponding log I versus log v of the Ni-PBA in 0.5 M $Al_2(SO_4)_3$ solution (The cathodic and anodic reaction of Ni-PBA electrode presented the b value of 0.68 and 0.75, respectively, indicating a Faradaic intercalation characteristic).
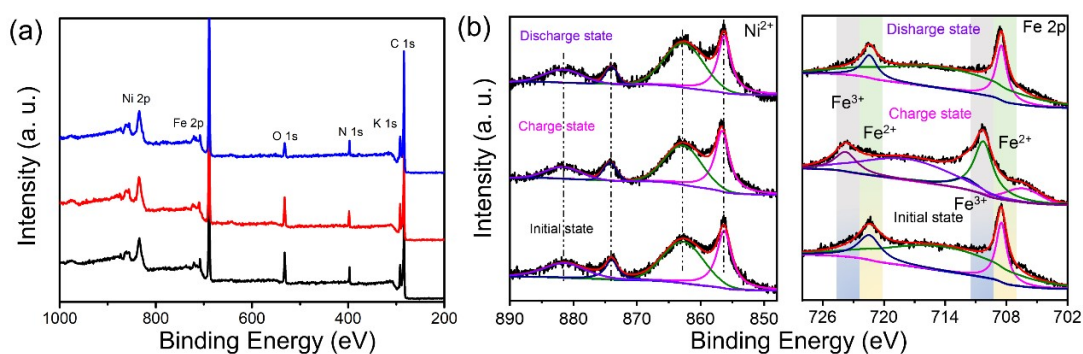

Figure. S15. (a) The full XPS survey spectra of Ni-PBA cathode at pristine (black line) and fully discharged (red line) and fully charged (blue line) states. (b) High resolution of Ni and Fe XPS spectrum at different state (In the initial state, the two characteristic Fe $2p_{3/2}$ and $2p_{1/2}$ peaks appeared at 708.5 and 721.5 eV, associated with the Fe^{II} state. In the charged state, the peaks related to Fe^{III} appeared at 710.2 eV and 723.7 eV while the Fe^{II} peaks disappeared, indicating that all Fe^{II} was oxidized to Fe^{III} with the extraction of K^+. At the subsequent discharged state, Fe^{III} became converted back to the original Fe^{II} oxidation state with the insertion of Al^{3+}. Nevertheless, the four Ni 2p peaks at about 881.7, 874.1, 862.8 and 856.5 eV remained almost constant during the charging/discharging processes, attributed to the Ni^{2+} ion being electrochemically inactive and just being used to maintain the stable framework of Ni-PBA).
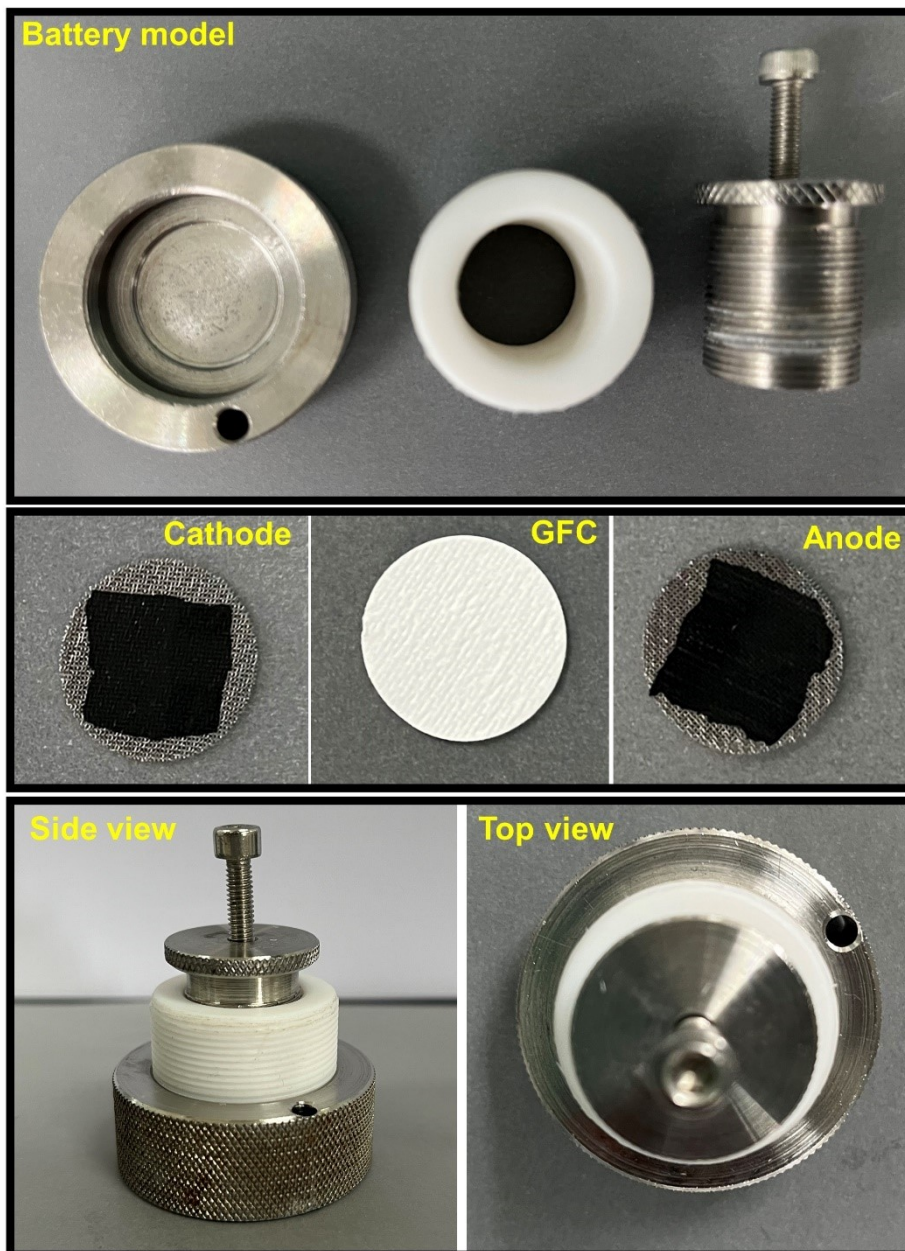
Figure S16. Digital images of full aqueous AIBs based on PBA cathode and PTO anode using the typical two-electrode configuration.

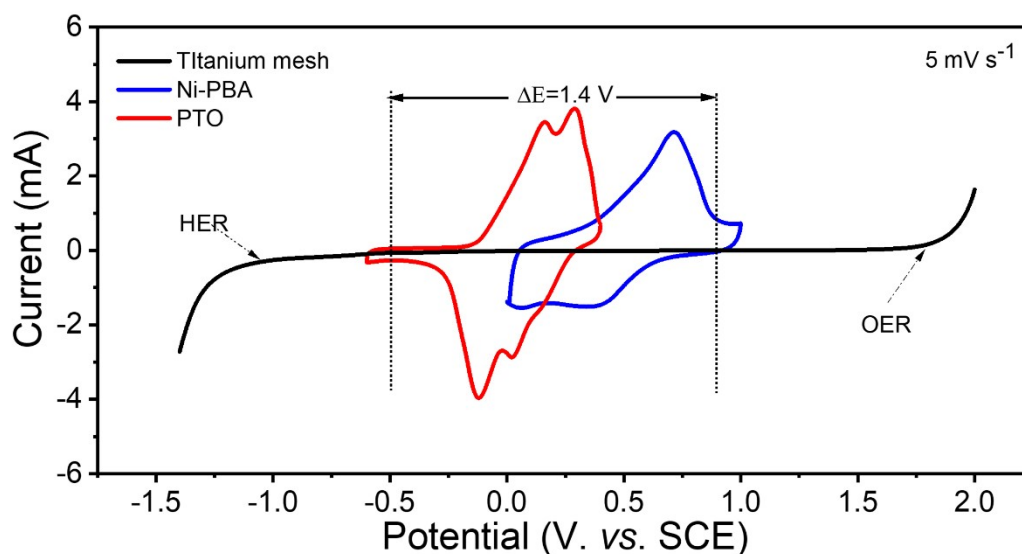**Figure S17.** Electrochemical windows and CV curves of the Ni-PBA cathode and PTO anode at 5 mV s^{-1} by using 0.5 M Al$_2$(SO$_4$)$_3$ solution (the redox potentials both for the two electrodes were located within the onset potential of oxygen evolution reaction and hydrogen evolution reaction).
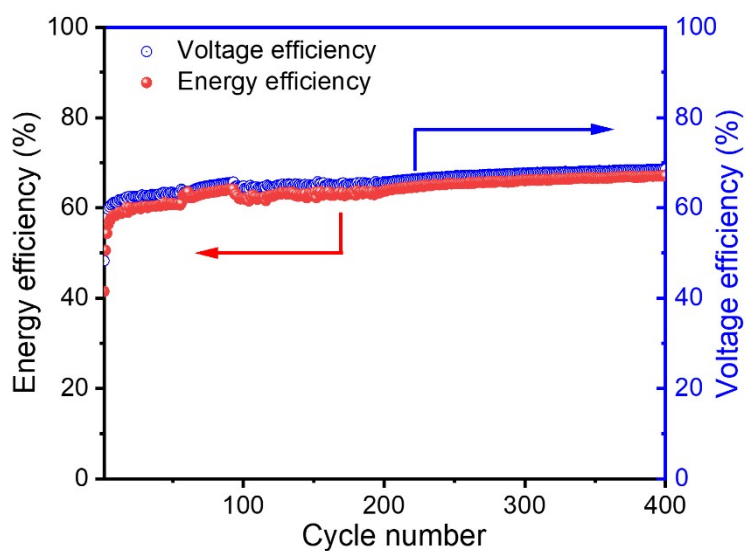

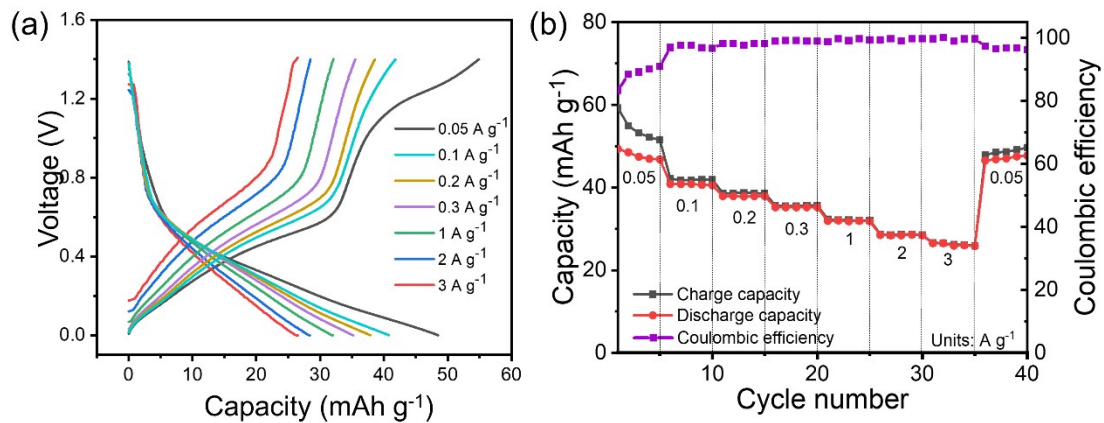**Figure S18.** Energy and voltage efficiencies of aqueous AIBs based on Ni-PBA cathode and PTO anode.

Figure S19. (a) The GCD curves and (b) rate performance of full aqueous AIB based on the Ni-PBA cathode and PTO anode at different current rates.
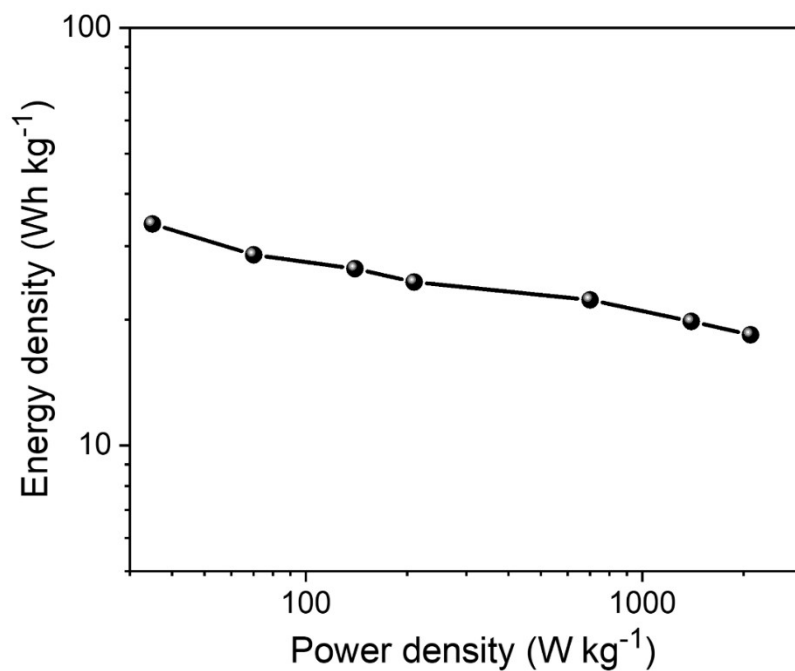

Figure S20. Ragone plot of aqueous AIBs based on Ni-PBA cathode and PTO anode.

Table S1 Comparison of Al^{3+} storage performance of other cathodes in aqueous electrolyte.

Cathode	Electrolyte	Initial capacity current density	Capacity retention	Ref.
$FeVO_4$	1 M $AlCl_3$	350 mAh g^{-1} at 0.06 A g^{-1}	14.2% after 20 cycles	[3]
VO_2	5 M $Al(OTf)_3$	73 mAh g^{-1} at 1 A g^{-1}	77.2% after 1000 cycles	[4]
$Na_3V_2(PO_4)_3$	1 M $AlCl_3$	120 mAh g^{-1} at 0.06 A g^{-1}	33.3 % after 20 cycles	[5]
$Al_{2/3}Li_{1/3}Mn_2O_4$	1 M $AlCl_3$ +1 M NaCl	138 mAh g^{-1} at 0.1 A g^{-1}	67.4 % after 1000 cycles	[6]
$K_2CuFe(CN)_6$	1 M $Al_2(SO_4)_3$	58.6 mAh g^{-1} at 0.5 A g^{-1}	75.3% after 500cycles	[7]
CuHCF	0.5 M $Al_2(SO_4)_3$	4.0 mAh g^{-1} at 0.4A g^{-1}	54.9 % after 1000 cycles	[8]
$K_2CoFe(CN)_6$	1 M $Al(NO_3)_3$	50.0 mAh g^{-1} at 0.1A g^{-1}	76.0% after 1000 cycles	[9]
Ni-PBA	0.5 M $Al_2(SO_4)_3$	61.6 mAh g^{-1} at 0.2A g^{-1}	85.4% after 1000 cycles	This work

Table S2 Comparison of the electrochemical performance with other rocking-chair aqueous multivalent-ion batteries

Rocking-chair aqueous batteries	Cathode	Anode	Electrochemical performance	Ref.
Zn^{2+}-ion	$ZnMn_2O_4$	$Na_{0.14}TiS_2$	An initial capacity of 38 mAh g^{-1} at 0.2 Ag^{-1} with capacity retention of 74.0% after 100 cycles	[10]
Ca^{2+}-ion	CaCuHCF	PNIDE	An initial capacity of 27 mAh g^{-1} at 0.4 A g^{-1} with capacity retention of 88.0% after 1000 cycles	[11]
Mg^{2+}-ion	$Na_{1.4}Ni_{1.3}Fe(CN)_6$	PI	An initial capacity of 35 mAh g^{-1} at 2 A g^{-1} with capacity retention of 60.0% after 5000 cycles	[12]
Al^{3+}-ion	CuHCF	PPy-MoO$_3$	An initial capacity of 31 mAh g^{-1} at 0.2 A g^{-1} with capacity retention of 83.2% after 100 cycles	[13]
Al^{3+}-ion	$VOPO_4$	MoO_3	An initial capacity of 80.1 mAh g^{-1} at 1 A g^{-1} with capacity retention of 86.2% after 2800 cycles	[14]
Al^{3+}-ion	$K_2CuFe(CN)_6$	AQ	An initial capacity of 53.2 mAh g^{-1} at 0.5 A g^{-1} with capacity retention of 89.1% after 100 cycles	[7]
Al^{3+}-ion	Ni-PBA	PTO	An initial capacity of 32.7 mAh g^{-1} at 1 A g^{-1} with capacity retention of 96.0% after 5000 cycles	This work

Supplementary Reference:

[1] Y. Liang, Y. Jing, S. Gheytani, K. Y. Lee, P. Liu, A. Facchetti and Y. Yao, *Nat. Mater.*, 2017, **16**, 841.

[2] M. Shi, C. Peng and X. Zhang, *Small.*, 2023, 2301449.

[3] S. Kumar, R. Satish, V. Verma, H. Ren, P. Kidkhunthod, W. Manalastas and M. Srinivasan, *J. Power Sources.*, 2019, **426**, 151-161.

[4] Y. Cai, S. Kumar, R. Chua, V. Verma, D. Yuan, Z. Kou, H. Ren, H. Arora and M. Srinivasan, *J. Mater. Chem. A.*, 2020, **8**, 12716-12722.

[5] F. Nacimiento, M. Cabello, R. Alcántara, P. Lavela and J. L. Tirado, *Electrochim. Acta.*, 2018, **260**, 798-804.

[6] R. Li, C. Xu, X. Wu, J. Zhang, X. Yuan, F. Wang, Q. Yao, M. Sadeeq Balogun, Z. Lu and J. Deng, *Energy Storage Mater.*, 2022, **53**, 514-522.

[7]] L. Yan, X. Zeng, S. Zhao, W. Jiang, Z. Li, X. Gao, T. Liu, Z. Ji, T. Ma, M, Ling and C. Liang, *ACS Appl. Mater & Interfaces.*, 2021, **13**, 8353-8360.

[8] S. Liu, G. L. Pan, G. R. Li and X. P. Gao, *J. Mater. Chem. A.*, 2015, **3**, 959-962.

[9] Y. Ru, S. Zheng, H. Xue and H. Pang, *Chem. Eng J.*, 2019, **382**, 122853.

[10] W. Li, K. Wang, S. Cheng and K. Jiang, *Adv. Energy Mater.*, 2019, **9**, 1900993.

[11] S. Gheytani, Y. Liang, F. Wu, Y. Jing, H. Dong, K. K. Rao, X. Chi, F. Fang and Y. Yao, *Adv. Sci.*, 2017, **4**, 1700465.

[12] L. Chen, J. L. Bao, X. Dong, D. G. Truhlar, Y. Wang, C. Wang, and Y. Xia, *ACS Energy Lett.*, 2017, **2**, 1115-1121.

[13] P. Wang, Z. Chen, Z. Ji, Y. Feng, J. Wang, J. Liu, M. Hu, H. Wang, W. Gan and Y. Huang, *Chem. Eng J.*, 2019, **373**, 580-586.

[14] P. Wang, Z. Chen, H. Wang, Z. Ji, Y. Feng, J. Wang, J. Liu, M. Hu, J. Fei, W. Gan and Y. Huang, *Energy Storage Mater.*, 2020, 25, 426-435.